Structural and Surface Studies of Luminescent Ca/Eu Phosphate Nanomaterials: From the Bulk to Surface Features

Pavlo Ivanchenko[1,2], Guillermo Escolano Casado[*1], Lorenzo Mino[1], Luca Dassi[1], Jorge F. Fernández-Sánchez[3], Gianmario Martra[1†], Jaime Gómez-Morales[4]

[1]Department of Chemistry and Interdepartmental Nanostructured Interfaces and Surfaces (NIS) Centre, University of Torino, via P. Giuria 7, Torino, 10125, Italy

[2]MOBI Research Group, Department of Electric Engineering and Energy Technology (ETEC), Vrije Universiteit Brussel, Pleinlaan 2, 1050 Brussels, Belgium

[3]Department of Analytical Chemistry, Faculty of Sciences, University of Granada, Avda. Fuentenueva s/n, 18071 Granada, Spain.

[4]Laboratorio de Estudios Cristalográficos. Instituto Andaluz de Ciencias de la Tierra (CSIC-UGR). Avda. Las Palmeras, nº 4. E-18100 Armilla (Granada), Spain.

[*]Corresponding author: guillermo.escolanocasado@unito.it

Abstract

Three luminescent Eu-containing phosphate materials (Ca-doped europium phosphate monohydrate, Eu-doped carbonated-apatite, and europium phosphate monohydrate) were prepared and analyzed on the level of bulk structure and surface properties and compared to the biomimetic non-luminescent counterpart hydroxyapatite. Europium-containing phosphate materials exhibited nanosized dimensions but different luminescence emissions and luminescence lifetimes depending on their crystalline structures (i.e., lanthanide phosphate or apatites) and chemical composition. The introduction of Eu in the crystal lattice leads to a notable decrease in the overall Lewis acidity of the surface cationic sites detected by CO probing. Further, the mixed Eu/Ca-containing materials surfaces were found to be very similar to the reference hydroxyapatite in terms of water adsorption energy, while the pure europium phosphate resulted to have the notably higher energy values of direct interaction of water molecules with the surface cations with no detected propagation of this effect towards water overlayers.

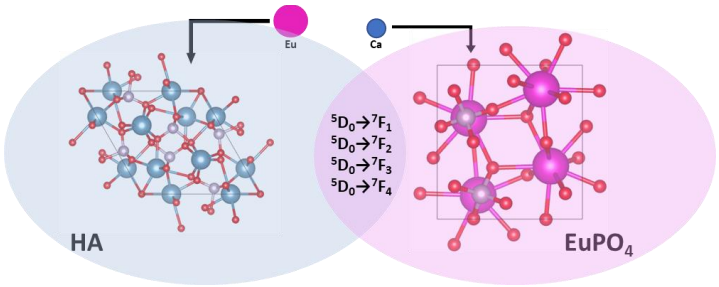

Introduction

Luminescent nanomaterials are very effective as optical probes for applications in biomedical imaging [1,2]. Materials of nanosized dimensions exhibit a set of unique magnetic, optical, and chemical properties largely diverging from their macro-scale counterparts. Thus, a good sensitivity, high contrast enhancement, signal-to-noise ratio, sharp emission peaks, high specific surface area, and controllable morphology along with a great photostability and chemical stability in a wide temperature and pH range, are characteristics of the luminescent nanomaterials that allow their use as probes for bioimaging. This set of properties can significantly enhance the capabilities of state-of-the-art fluorophores (i.e., genetically engineered proteins or luminescent organic dyes). In this context, metal quantum dots, nanodiamonds [3], carbon nanomaterials[4,5], and recently lanthanide-substituted calcium orthophosphate apatites (Ln^{3+}:Ap; Ln^{3+}=Eu^{3+}. Tb^{3+}, Ce^{3+}[6] have been studied concerning their bioimaging applications.

The fate of an interaction of a nanomaterial with the biological media lies in the surface structure of a material [7]. Different surfaces may interact with the components of a medium, such as water, and biomolecules having an effect on the adsorption state of these components 'attached' to the surface thus causing differences in the response of living cells. In this respect, hydroxyapatites were found to possess excellent biocompatibility [8]. Apatites, as host materials, are structurally similar to the inorganic components of bone and teeth, and present excellent properties such as crystal structural flexibility, ability to include many different dopant ions, biocompatibility, bioactivity, biodegradability, and absence of inflammatory and immune responses [9]. In addition to these materials, lanthanide orthophosphates ($LnPO_4.nH_2O$ (n = 0–2) have emerged as new candidates for this type of application thanks to their low cytotoxicity [10], low solubility in water, and high refraction index. Lanthanide orthophosphates present five polymorphic modifications including monazite (monoclinic), xenotime (tetragonal), weinschenkite (monoclinic), an orthorhombic phase, and the low-temperature phase rhabdophane (hexagonal) [11]. Regardless of the chemical nature and crystallographic structure of the nanomaterials hosting the lanthanides (apatites or lanthanide phosphates), these luminescent ions provide large effective Stokes shift, sharp emission peaks with narrow bandwidth, color tuning depending on the type of lanthanide ion, and long luminescence lifetimes along with the high stability to photochemical degradation and photobleaching [10,12,13].

In general, Ln^{3+}-containing phosphates (apatites or lanthanide phosphates) compared with luminescent carbon nanomaterials (i.e., carbon dots) in that both types of phosphors exhibit strong luminescence, stability against photobleaching and do not show photoblinking or remarkable cytotoxic effects [5,6]. Metal-free systems like these show interest from both scientific and commercial sides due to the high versatility of possible nanoparticles structures uniting carbon atoms in sp^2 and sp^3 hybridization, the high flexibility for the functionalization, thus opening broad possibilities for tuning their biological (biomimetic), catalytic (enzyme-mimicking[14]), and optical (luminescent[5]) properties, and also because of the variety of carbon sources that can be used for its preparation. On the other side, the main advantage of Ln^{3+}-containing phosphates nanomaterials concerning metal-free systems is the possibility of tuning their luminescence by varying the heteroatom content in the bulk structure[15,16], thus avoiding the use of adsorbed organic dyes. Once adsorbed on the nanoparticles surface, the organic dyes tend to change their surface features (i.e., hydrophilicity, surface charge) and so the way of interaction of the nanoparticles with the biological media. The role of heteroatoms was also highlighted in materials for different applications[17,18].

Among lanthanides, europium (III) has been one of the most widely used to fabricate luminescent nanoparticles for biological applications, exploiting the luminescent 4f–4f transitions in the visible region, leading to the emission of red luminescence [19–23].

Biomimetic and bioinspired europium-containing phosphate nanoparticles such as europium-doped carbonated apatite (**HA-Eu**), europium phosphate monohydrate (**EuP**), and calcium-doped europium phosphate monohydrate (**EuP-Ca**), the last two of the rhabdophane phase, have been previously prepared by the citrate-based thermal decomplexing method at 80 °C, and widely investigated in respect to their luminescent properties and cytocompatibility, highlighting their potential applications in the field of bioimaging [1,12]. For these applications, the knowledge of their surface properties such as hydrophilicity or Lewis acidity is important to predict the interaction of the nanoparticles with biological aqueous fluids components.

In this work, we investigate and compare the surface properties of these nanoparticles with a focus on the surface composition, Lewis acidity, and water adsorption capacity, as well as their bulk structure and luminescent properties.

2. Materials and Methods

Materials synthesis

The following reagents were purchased from Sigma-Aldrich: Calcium chloride dihydrate ($CaCl_2 \cdot 2H_2O$, Bioxtra, 99.0% pure), europium chloride hexahydrate ($EuCl_3 \cdot 6H_2O$, ACS reagent, 99.9% pure), sodium citrate tribasic dihydrate ($Na_3(C_6H_5O_7) \cdot 2H_2O$, ACS reagent, ~99.0% pure), disodium hydrogen phosphate (Na_2HPO_4, ACS reagent, ~ 99.0% pure), sodium carbonate monohydrate ($Na_2CO_3 \cdot H_2O$, ACS reagent, 99.5% pure) and hydrochloric acid (HCl, ACS reagent, 37 wt.% in H_2O). All solutions were prepared with ultrapure Milli-Q water (0.22 mS, 25 °C, Millipore).

The experiments were carried out by thermal treatment of metastable solutions containing Eu^{3+}/Ca^{2+}-citrate complexes in the presence of phosphate and carbonate ions, at pH = 8.5 [1,12]. In brief: two solutions of compositions (a) 0.12 M Na_2HPO_4, + 0.2 M Na_2CO_3 and (b) *x* M $EuCl_3$ + *y* M $CaCl_2$ + 0.4 M Na_3(cit), with *x* = 0.1 M and *y* = 0 for sample **EuP**, *x* = 0.01 M and *y* = 0.09 M for sample **HA-Eu**, and *x* = 0.09 M and *y* = 0.01 M for sample **EuP-Ca**, with the pH adjusted to 8.5 with diluted HCl, were mixed (1:1 v/v) at 4 °C in a 100 mL Pyrex glass bottle, sealed with screw cap, and immediately immersed in a water bath at 80 °C. Then, the bottle was moved to an oven with circulated forced air at the same temperature for 7 days. The precipitates were subjected to 6 cycles of washing by centrifugation with Milli-Q water to remove unreacted salts. Afterward, they were dried at 37 °C for 2 days in an oven with circulated forced air.

X-ray diffraction

X-ray diffraction (XRD) patterns of the powders were recorded with an Analytical X'Pert Pro equipped with an X'Celerator detector X-ray powder diffractometer using Cu Kα radiation generated at 40 kV and 40 mA. The instrument was configured with 1/2° divergence and receiving slits. A quartz sample holder was used. The 2θ range was from 5° to 60° with a step size (2θ) of 0.05° and a counting time of 3 s.

The 002 and 310 reflections were considered to calculate the average size of crystal domains (*d*) in hydroxyapatite along the [002] and [310] directions, respectively, by the Scherrer equation:

$$d = \frac{K\,\lambda}{(B_{exp} - B_{ins})cos\theta} \qquad (1)$$

where *K* is a shape factor (assumed to be 0.9 in the present case), λ is the X-ray wavelength, θ is the measured Bragg angle, and B_{exp} and B_{ins} are the experimental and instrumental broadening, respectively. The instrumental broadening was evaluated using a Si powder standard [24].

High-Resolution Transmission Electron Microscopy

High-resolution transmission electron microscopy (HR-TEM) images of the materials (powder grains dispersed on Cu grids coated with a lacey carbon film) were obtained with a JEOL 3010-UHR operated at an acceleration potential of 300 kV. As apatite samples might evolve under the electron beam, potentially leading to further crystallization and/or a loss of bulk water, observations were conducted under feeble illumination conditions to avoid any modification of the materials during the analysis. Fourier transforms of direct images were performed using the Gatan Digital Micrograph program software.

Specific Surface Area measurements

Specific surface area (SSA) was measured with a Micromeritics ASAP 2020 by nitrogen adsorption at 77 K following the BET model. For the measurements, the materials were outgassed at room temperature for at least 12 h (final residual pressure of 1×10^{-3} mbar).

Luminescence spectroscopy

The luminescence properties of the solid europium-containing particles (luminescence spectra, luminescence lifetime (τ) and the relative luminescence intensities (R.L.I)) were recorded with a Cary Eclipse Varian Fluorescence Spectrophotometer (Varian Australia, Mulgrave, Australia), using a front surface accessory. The instrumental parameters for characterizing the solid particles were: λ_{exc}= 225 nm, λ_{em}= 614 nm, slit-width $s_{exc/em}$= 10/10 nm, delay time (td)= 0.120 µs, gate time (t_g)= 5 ms and detector voltage= 500 V. Luminescence lifetimes (τ) were measured using the following conditions: $\lambda_{exc/em}$=225/614 nm, slit-width $s_{exc/em}$= 10/10 nm, t_d= 0.1 µs, t_g=0.1 ms and detector voltage= 550 V.

Fourier Transform Infrared analysis

FT-IR spectroscopy in a controlled atmosphere was used for inspecting surface features. For this, nanoparticles were pressed in the form of self-supporting pellets and placed into an IR cell equipped with KBr windows allowing to cool down the sample to the temperature of liquid nitrogen (ca. 77 K) and connected to a conventional vacuum line (residual pressure 5×10^{-4} mbar), allowing adsorption/desorption experiment to be carried out in situ. The IR spectra were collected in the transmittance mode with an Equinox 55 spectrometer (Bruker, Karlsruhe, Germany) equipped with a DTGS detector (128 scans; resolution: 4 cm^{-1}).

Microcalorimetric studies

The calorimetric H_2O adsorption-desorption measurements were carried out in situ, all the thermal treatments were done in vacuo. The samples (pressed in self-supporting pellets) were outgassed at 433 K

for 2 h (residual pressure p ≤10^{-4} mbar) before the water adsorption measurements. The enthalpy change associated with the adsorption was measured at 303 K with a heat-flow microcalorimeter (Calvet C80, Setaram, F) connected to the custom high-vacuum gas-volumetric gas apparatus (residual pressure p≤10^{-4} mbar). A previously established procedure was employed [25]; it allowed to determine the adsorbed amounts and integral heats evolved as the function of equilibrium pressure (monitored by Ceramicell 0-133.33 mbar, Varian) along with small increments of the adsorptive. The maximum water vapor pressure in equilibrium was limited to 10 mbar, a conservative value for effective use of the perfect gas law for the data elaboration. The calorimetric outputs (integral heats evolved during the adsorption, Q^{int}) were processed to obtain the differential heats of adsorption ($q_{diff} = -\Delta_{ads}H$, kJ·$mol^{-1}$), that allows quantifying accurately the energy of interaction of a molecular probe with the individual surface sites.

Results and discussion.

1. Structural characterization

General structural insights into the synthesized samples were obtained by X-ray diffraction (**Figure 1**). The EuP and EuP-Ca show the characteristic XRD peaks of $EuPO_4 \cdot H_2O$ (PDF card #00-020-1044), while the HA-Eu data are compatible with the pattern of a single-phase hydroxyapatite (PDF card # 00-009-0432). The XRD peaks are quite broad in agreement with the nanocrystalline character and high BET specific surface area (SSA_{BET}) of the particles (***Table 1***). For HA-Eu, the pattern is similar to pure nanometric HA samples synthesized in presence of citrates [14]. In particular, an elongation of the coherent scattering domains along the *c*-axis of the HA hexagonal structure can be noticed. Indeed, applying the Scherrer analysis (equation 1) to the peaks at 25.8° (002 reflection) and 39.8° (310 reflection), a crystal domain size of 7 nm can be estimated along the [310] direction, while along the [200] direction this increases to 17 nm.

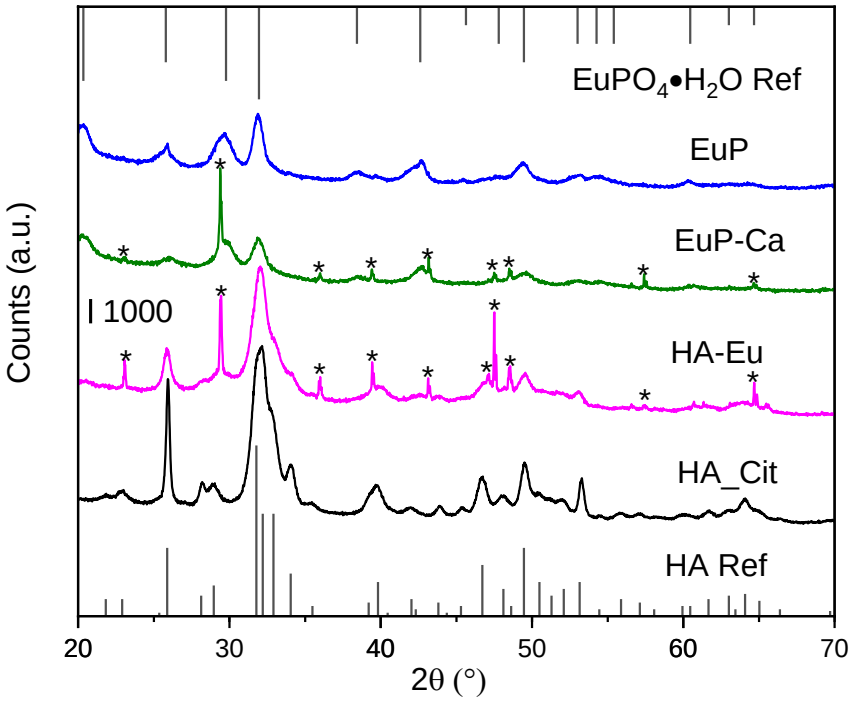

Figure 1. XRD patterns of the EuP, EuP-Ca, and HA-Eu particles. The pattern of similar pure hydroxyapatite synthesized using citrates (HA_Cit [26]) is also reported. Peak positions and relative intensities (vertical lines) of hydroxyapatite (HA Ref, PDF card #00-009-0432) and ($EuPO_4 \cdot H_2O$, PDF card #00-020-1044) are shown for comparison. An asterisk marks the main XRD peaks due to the presence of calcite.

Finally, for both samples containing calcium, we can also notice the presence of XRD peaks assigned to a $CaCO_3$ (calcite) phase (marked by an asterisk in **Figure 1**). The presence of calcite in HA-Eu and EuP-Ca samples can affect the calculation of the SSA_{BET} values which are employed for quantitative estimations of the water adsorption (*vide infra*) as the normalization factor between different samples. However, the sharpness of the XRD peaks suggests that the calcite particle size is in the micrometric range, i.e., much bigger compared to the size of the phosphatic nanoparticles. This evidence and the limited amount of calcite contained in the samples (around 5.5 wt.%, see ***Table 1***) suggest that this phase is not significantly influencing the SSA_{BET} measurements. However, to estimate the SSA_{BET} more realistically, the SSA_{BET} values were recalculated with the calcite estimated mass excluded from the measured outgassed sample weight. The results of these manipulations are presented in ***Table 1*** along with the deviations (in %) of the estimated SSA_{BET} of the powder excluding the calcite concerning the SSA_{BET} of the 'full' sample. Given that the intrinsic experimental error of the BET model is around 10%, these evaluations do stay close to the margin of error evidencing the limited effect of the presence of the calcite over the further spectroscopic and gravimetric measurements having very low sensitivity to the low SSA_{BET} materials.

Table 1. Measured BET specific surface area (SSA_{BET}) for the different materials and estimated SSA_{BET} excluding the calcite contribution.

Material	Measured SSA_{BET} (m^2/g)	Calcite (wt%)	Estimated SSA_{BET}	SSA deviation, %
HA-Eu	171	5%	180	5.2%
EuP-Ca	108	5%	114	5.6%
EuP	120	n/a	120	n/a

Complementary dimensional and structural analysis was then performed by electron microscopy. Low magnification images (**Figure S1**) further confirm that the calcite particles are of micrometric dimension and, thus, do not contribute significantly to the SSA_{BET}. **Figure 2** highlights that the nanoparticles show an elongated morphology along the *c*-axis, preferentially exposing {010} facets, in agreement with the XRD results. High-resolution TEM images of the EuP and EuP-Ca samples show interference fringes with d = 5.216 Å, compatible with the {101} interplanar distances of the rhabdophane crystal structure.

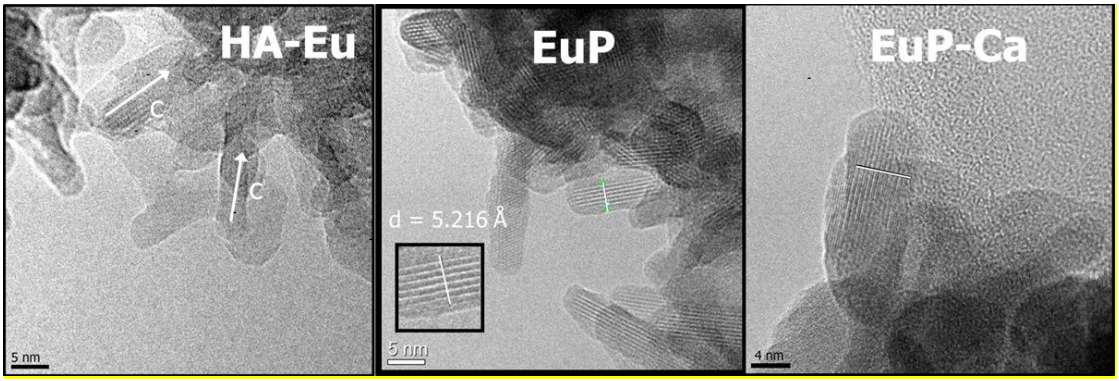

Figure 2. HR-TEM images of the HA-Eu, EuP, and EuP-Ca samples. Interferences fringes are evidenced by a white bar in EuP and EuP-Ca. Finally, the inset in EuP shows the interplanar distance with d = 5.216 Å.

The presence of $CaCO_3$ (calcite phase) in HA-Eu and EuP-Ca samples was a source of propagating errors at further quantitative estimations of the water adsorption (SSA values considered as the normalization factor between different samples). As evidenced by the XRD and TEM, the size of the calcite particles is vast, compared to the size of the phosphatic nanoparticles. This fact causes a comparatively negligible area of calcite being around 5.5 % of the weight of a sample (order of $<1 m^2/g$ for the micron-sized particles) is contributing to the measured SSA values. To estimate the SSA more realistically, the SSA values were recalculated by the means of Micrometrics software with the calcite estimated mass excluded from the measured outgassed sample weight. The results of these manipulations are presented in ***Table 1*** along with the deviations (in %) of the estimated SSA of the powder excluding the calcite concerning the SSA of the 'full' sample. Given the intrinsic experimental error of the ASAP-2020 instrument is around 10%, these evaluations do stay close to the margin of error evidencing the limited effect of the presence of the calcite over the further spectroscopic and gravimetric measurements having very low sensitivity to the low SSA materials.

2. Luminescence spectra, relative intensities, and lifetimes

The luminescence properties of HA-Eu, EuP, and EuP-Ca samples in a solid state are shown in **Figure 3**. The sensitized luminescence [12,27] excitation wavelengths are 225, 320, 364, 382, and 396 nm, and emission wavelengths are 592, 614, 654, and 700 nm.

The broad excitation band between 200 and 290 nm corresponds to charge transfer (CTB), which occurs by electron delocalization from the filled 2p shell of O^{2-} to the partially filled 4f shell of Eu^{3+}. Also, this band can partly be attributed to the charge transfer transition X^{5+}–O^{2-} [28–30]. The rest of the excitation bands correspond to the Eu^{3+} $^7F_0 \rightarrow {}^5H_6$, $^7F_0 \rightarrow {}^5D_4$, $^7F_0 \rightarrow {}^5L_7$, and $^7F_0 \rightarrow {}^5L_6$ transitions, while the emission bands correspond to the Eu^{3+} $^5D_0 \rightarrow {}^7F_1$, $^5D_0 \rightarrow {}^7F_2$, $^5D_0 \rightarrow {}^7F_3$ and $^5D_0 \rightarrow {}^7F_4$ transitions, respectively [31].

The maximum luminescence excitation and emission wavelengths are 224/614 nm which corresponds to the CTB band and the hypersensitive transition without inversion center which results in the highest relative luminescence intensity (R.L.I) when nanosized particles dominate the luminescence emission [32].

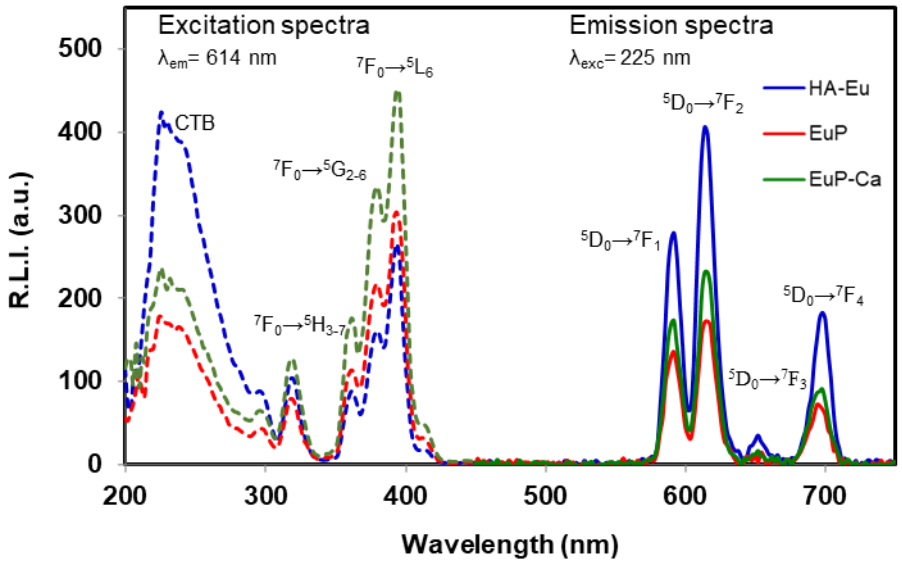

Figure 3. Uncorrected excitation (dashed lines) and emission (solid lines) spectra of different HA-Eu (blue), EuP (red) and EuP-Ca(green) particles. Slit-width$_{sexc/em}$ = 10/10 nm, t_d = 120 µs, t_g = 5 ms and voltage detector = 500v.

Concerning the comparison of the luminescence emissions, it shows that HA-Eu displays the highest R.L.I. while EuP-Ca and EuP have R.L.I. more similar between them. This finding can be interpreted by the difference in crystalline structures and chemical compositions of the europium-containing particles; thus, nanoparticles of the apatite phase are providing the highest emission whereas those of the rhabdophane phase show the lowest ones. In addition, the doping with Ca^{2+} (i.e. EuP-Ca sample) increased the luminescence emission; as was already previously reported [1,12].

Figure 4 shows the luminescence lifetime (τ) of these materials. For each sample, the decay profile was analyzed as a single exponential component (R.L.I. = $A \cdot e^{-t/\tau} + C$) [33].

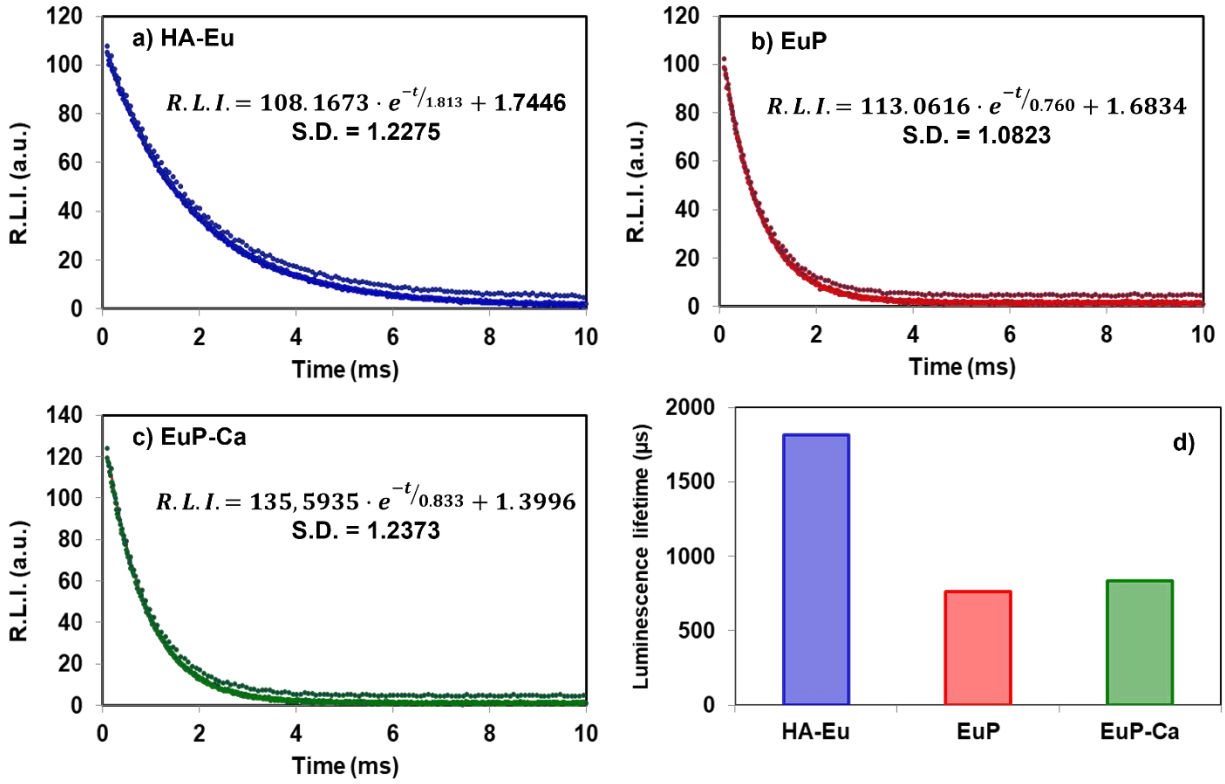

Figure 4. Luminescence decay curve of a) HA-Eu, b) EuP and c) EuP-Ca, and d) comparison of the luminescence lifetimes. $\lambda_{exc/em}$ = 225/614 nm, slit-width$_{sexc/em}$ = 10/0 nm, and detector voltage = 550 V. Dotted lines correspond to experimental data and lines to the fitting equation

The highest lifetime is shown by the apatitic sample (1800 µs) while the two rhabdophane samples (EuP and EuP-Ca) show lifetimes of approx. 800 µs, but slightly higher for the Ca^{+}-doped sample. It was also observed previously [1,12].

3. Surface characterization.

The IR spectral profile of citrates molecules present at the EuP nanoparticles collected in presence of water vapor pressure (**Figure 5A**, curve a) is characterized by 2 distinct bands of antisymmetric stretching mode around 1600 cm^{-1} (ν_{asym}) and symmetric stretching mode around 1400 cm^{-1} and another one lower in intensity at ca. 1440 cm^{-1} (ν_{sym}) of COO^{-} moieties [34–36]. However, the presence of water multilayers affects the spectral profile by contributing a band due to δHOH at ca. 1645 cm^{-1} and by modifying an overall refraction index of the system [26]. The removal of reversibly adsorbed water by 1 h outgassing at beam temperature (**Figure 5A**, curve b) improves the visibility of the carboxylate modes (**Figure 5A**, curve b). However, the δHOH due to irreversibly adsorbed water is still present as a shoulder of the $\nu_{asym}COO^{-}$ mode; its removal after 5 cycles of H/D exchanges and outgassed for 1 hour reveals the exact shape and position of the citrates IR band (**Figure 5A**, curve c). This experimental approach allowed us to appreciate the shape of the IR bands of the citrate species present at the surface free from the contribution of water in the final shape of the spectra. Thus, the citrate profile in the part of carboxylates antisymmetric

stretching mode consists of 2 distinct sub-bands of similar intensities located at ca. 1600 cm^{-1} and 1577 cm^{-1}, while the carboxylate symmetric stretching mode exhibits overall lower intensities and also consists of at least 2 well-resolved components: one higher intensity sub-band at ca. 1400 cm^{-1} and a lower intensity component at ca. 1440 cm^{-1}.

Comparing the 2 profiles of carboxylates adsorbed on HA (**Figure 5A**, curves c and d), it is worth noting that the two modes coincide very well in terms of the position. In terms of the shape of the antisymmetric stretching mode of COO^- of EuP-bound citrates is slightly broader and has a better-pronounced sub-bands compared to the corresponding bands of the citric acid bound to the surface of HA. Further, the overall shape of the symmetric stretching modes of carboxylates is very similar for the two samples with the only difference being the higher overall intensity in the case of EuP material.

The relative position of the $\nu_{asym}COO^-$ and $\nu_{sym}COO^-$ in terms of $\Delta\nu$ assigned to carboxylate species interacting with metal ions is known to be sensitive to the type of bonding: ionic, monodentate, chelating, or bridging affecting the splitting gap [35]. On this basis, we can assume that similar to the HA system discussed in detail in our previous work, (**Figure 5A**, curve d – adapted from the ref. [26]), citrates adsorbed on the EuP also seem to exhibit monodentate coordination to the surface Eu cations.

Unlike EuP, neither of the Ca-containing samples evaluated within this study were found to have surface-bound citrates. Conversely, EuP-Ca and HA-Eu were found to contain the band due to carbonate species [37] (**Figure 5B**, curves a and b) likewise the 'pure' HA [38,39] (**Figure 5B,** curve c). The carbonate band of a reference hydroxyapatite material (**Figure 5B**, curve c) is composed of two overlapping components that for HA samples can be ascribed as type A (at higher wavenumbers) and type B (at lower wavenumbers) carbonates resulting from the substitution of hydroxyls and phosphates, correspondingly. Regardless, the carbonate band of EuP-Ca material exhibits a similar overall shape and position, this assignment cannot be applied in this case, since EuP-Ca intrinsically has no hydroxyl groups in the bulk or on the surface. We can assume that the division of the carbonate species into two sub-bands might originate from the relative vicinity of the carbonate groups to either Ca^{2+} or Eu^{3+} in the bulk structure. To monitor the exposure of the carbonate species to the surface, the spectra of the materials in presence of D_2O were collected (**Figure 5B**, curves a' and b'). When (heavy) water interacts with the carbonate species, it perturbs the latter ones resulting in a higher extinction coefficient, thus increasing in intensity (like in **Figure 5B**, curves c and c'). The ascribed behavior was observed for the sample HA-Eu (**Figure 5B**, curves b and b'), evidencing the exposure of both type A and type B carbonates to the surface. However, the EuP-Ca sample did not have that well-pronounced perturbation (**Figure 5B**, curves a and a'). It allows us to deduce that the carbonate species present in the material have negligible exposure to the surface.

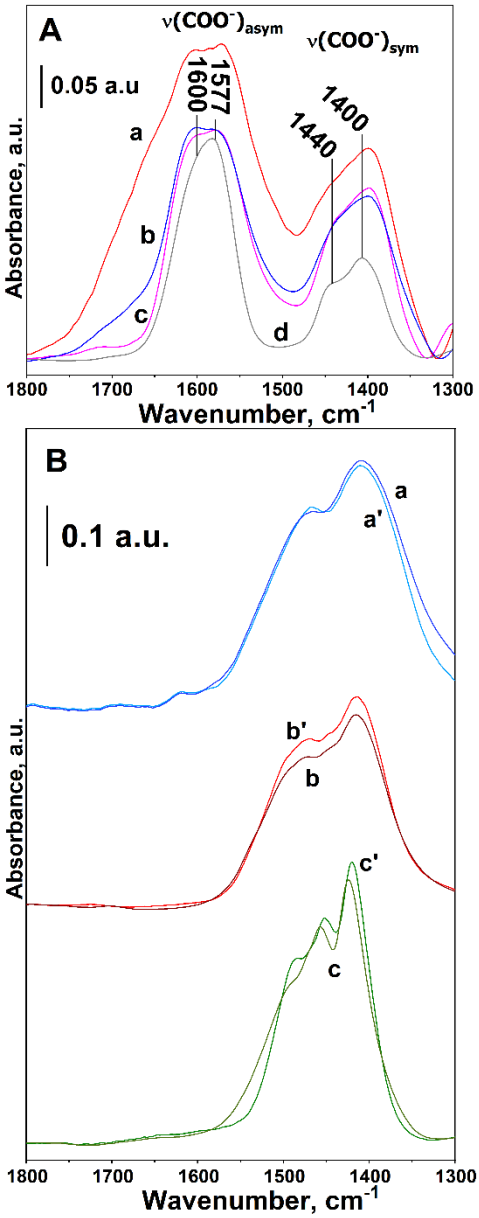

Figure 5. Panel A: FTIR spectra of EuP sample in presence of 22.5 mbar of water vapors (curve a), the same sample after 40 min outgassing at b.t (residual pressure $1 \cdot 10^{-3}$ mbar – curve b), and after cycles of H/D exchange and consequent outgassing until invariance of the spectra (curve c). Curve d refers to the HA sample after cycles of H/D exchange and outgassing till invariance of the spectra, adapted from the ref. [26]. **Panel B:** Carbonate bands of EuP_Ca (curve a), HA-Eu (curve b), and the Pure HA sample from the previous works by some of us (curve c – [40]) after the H/D exchange and outgassing till invariance of the spectra, the curves a', b', and c' are the same samples in presence of 22.5mbar of D_2O.

To obtain insights into the properties of the surface-exposed cations, the in-situ controlled low-temperature adsorption of CO was adsorbed [41]. To probe the surface Eu^{3+} and Ca^{2+} ions by Infrared spectroscopy, water molecules left irreversibly adsorbed after outgassing at room temperature, had

to be removed at a higher temperature. To limit the effect of the thermal treatment on the surface structure combined with the effective water desorption, a series of preparatory measurements was carried out (further experimental details are reported in SI). Based on these tests, it was found that the lowest temperature necessary to remove all the residual water from the surface of EuP and HA-Eu is 373 K, while for the EuP-Ca it is 423 K (see **Figure S1** in SI).

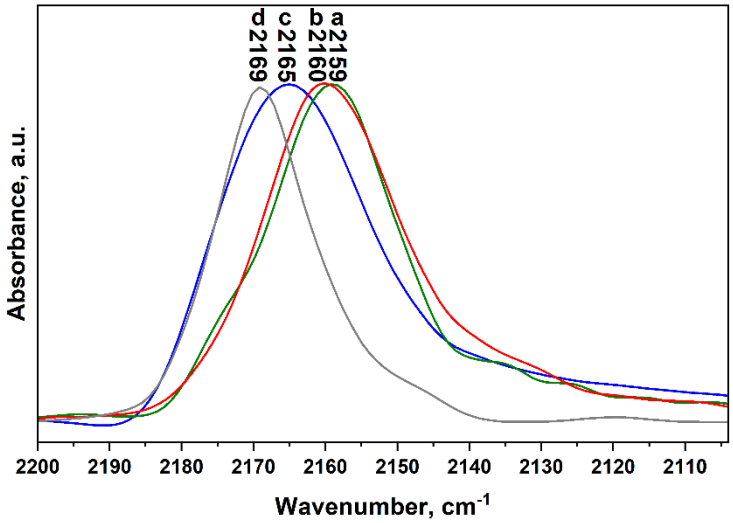

Figure 6. FTIR spectra resulting from the subtraction of the spectra of CO adsorbed on EuP (curve a), HA-Eu (curve b), EuP-Ca (curve c), and HA (adapted from the ref [40]) in equilibrium with 20 Torr at ca.77 K with the sample before the admission of CO. All samples were pre-outgassed at 433 K under outgassing to remove irreversibly adsorbed water (residual pressure p = 10^{-3} mbar). For the sake of comparison, the intensities were normalized to the value of 1.

CO stretching mode is known to be highly sensitive (in terms of the position and shape) to the Lewis acidity of the surface cation it is interacting with. Thus, the shape and position of νCO observed for EuP and HA-Eu samples (**Figure 6**, curves a and b) exhibit very similar shapes, and the position of the band maxima being 2159 cm^{-1} and 2160 cm^{-1}, correspondingly. It is worth noting that the probe molecules are in contact only with the part of the surface free from irreversibly adsorbed citrates. Next, the CO adsorbed on EuP-Ca gives rise to the band centered at ca. 2165 cm^{-1} (**Figure 6**, curve c) exhibiting a width similar to those of EuP and HA-Eu. Interestingly, in the case of pure HA (**Figure 6**, curve d – adapted from the ref. [40]) the νCO mode is located at the highest wavenumber and exhibits a noticeably narrower shape in the series. The position of the CO adsorption maximum is an important parameter to consider concerning Lewis acidity. Thus, the difference between the wavenumbers of the νCO in adsorbed state and the gas phase (being 2143 cm^{-1}) is greater for the stronger Lewis acid sites. On such a basis, the overall Lewis acidity of the surface cations could be ordered in the following sequence HA > EuP-Ca > HA-Eu ≥ EuP (see details in ***Table S1***).

Apart from that, the width of νCO profile may be an indicator of the greater number of the 'families' of the surface sites, being more homogeneous for the pure HA and resulting in the greater distribution in terms of Lewis acidity strength for the rest of the samples in the series.

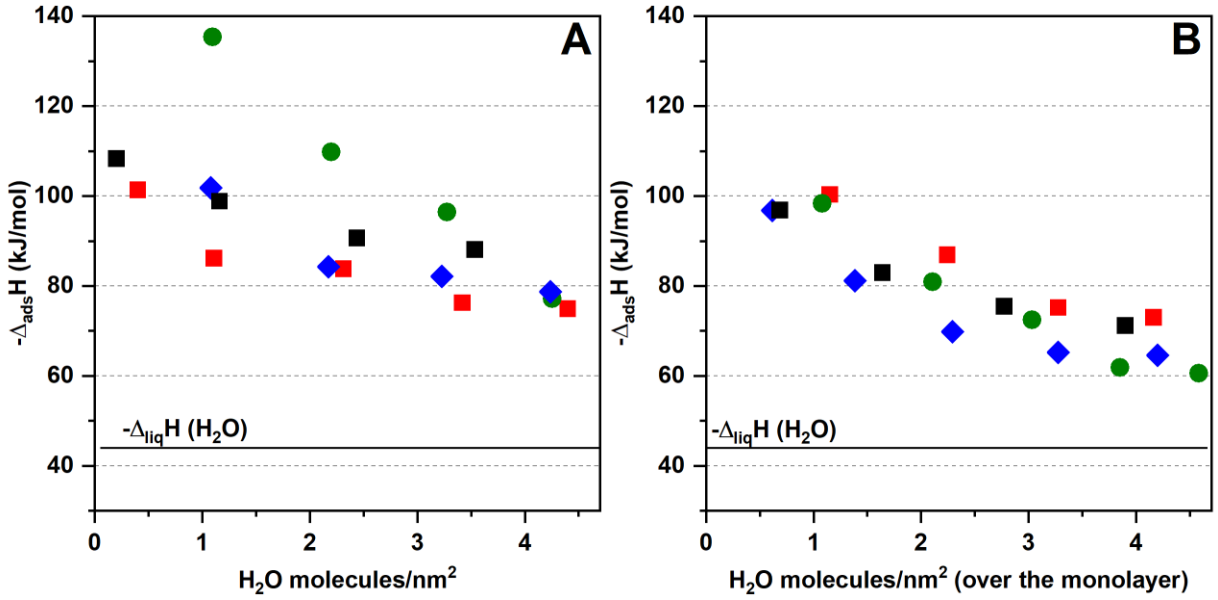

Figure 7. Adsorption enthalpies of the adsorption plotted versus the water molecules uptake (in terms of a number of molecules per nm^2): green symbols – EuP, blue – EuP-Ca, red – HA-Eu, black – HA [26]; Panel A: the samples pre-outgassed at 423 K (2 h), Panel B: samples pre-outgassed at 298 K (overnight); the black horizontal line indicates the value of latent enthalpy of liquefaction of water, ($-\Delta_{liq}H$ (H_2O) = 44 kJ/mol) for the sake of comparison.

To investigate the energetic aspects of water adsorption in terms of adsorption enthalpies ($-\Delta_{ads}$) the series of microcalorimetric measurements were performed by admitting small portions of the water vapor over the three samples and compared to the previously studied HA (**Figure 7**).

It is worth noting that the attaining of the first hydration layer on EuP-Ca and HA-Eu (**Figure 7**, panel A, blue and red symbols) is characterized by very similar energetic profiles ($-\Delta_{ads}H$ of the first admission portion being between 100 and 110 kJ/mol), also overlapping with the pure HA sample (**Figure 7**, panel A, black symbols). On the other hand, the energetic behavior of water molecules contacting directly with the surface of EuP is noticeably different (starting from ca. 138 kJ/mol), meaning the greater values of the enthalpy at the beginning of water admission meaning the greater polarization effect on water molecules. Intrinsic rhabdophane structure contains hydrated Eu ions; thermal pre-treatment at 423 K could (partially) dehydrate the surface cations, thus first portions of water may be involved in complexation reaction [1]. However, upon attaining the monolayer coverage, the enthalpy values of EuP are comparable to those of EuP-Ca and HA-Eu, being below 80

kJ/mol. Further, the adsorption of water overlayers on all of the samples follows a very similar energetic behavior (**Figure 7,** panel B), resulting in the water-water interaction being significantly stronger than for liquid water (enthalpy of water liquefaction $-\Delta_{ads}H$ = 44 kJ/mol [25,42]). This behavior can be attributed to the strong affinity of Eu/Ca surface sites to water in all the considered materials.

Conclusions

Citrate-coated $EuPO_4 \cdot H_2O$ nanoparticles result to exhibit rhabdophane phase, high specific surface area, and lower Lewis acidity compared to apatites. Infrared spectroscopic study of the coordination of citrates bound to the surface of europium phosphate nanoparticles evidenced a monodentate type of binding. Regardless of the co-precipitation of a notable amount of calcite particles, the mutual Ca^{2+}/Eu^{3+} substitutions resulted in the formation of stable crystalline phases, both containing carbonate groups in their crystalline structures, being partially exposed to the surface of the Eu-containing HA sample. On the other hand, there is no spectroscopic evidence of the exposure of the carbonates to the surface of Ca-containing europium phosphate.

Further, the introduction of europium in the phosphate crystal matrix resulted in a decrease in the surface Lewis acidity within the set of studied materials. However, regardless of different cationic compositions, both Ca^{2+}/Eu^{3+} mutually exchanged materials exhibit very similar water adsorption energies, being close to that found in the biomimetic apatite, while Europium phosphate exhibits high energy in the formation of the first hydration layer, turning very close to the biomimetic materials upon attaining a monolayer coverage.

Concerning the luminescence properties of the Eu^{3+}-containing nanoparticles, they all exhibit similar luminescence spectra (i.e., similar excitation and emission wavelengths), characteristic of the presence of Eu^{3+} in the samples, but different R.L.I. and luminescence lifetimes of the apatite and rhabdophane phases, revealing the influence of the host matrix structure. All of them display suitable luminescent properties for their use in bioimaging.

Acknowledgements

This work is dedicated to our teacher, colleague, and friend Gianmario Martra who left us too soon and never said nothing. We know he is going on ahead and that he is fixing to make a fire somewhere out there in all that dark and all that cold.

Funding

This work was supported by projects PGC2018-102047-B-I00 (MCIN/AEI/FEDER, UE) and PCI2020-112108 funded by MCIN/AEI/10.13039/501100011033 and the European Union "NextGenerationEU"/PRTR". PCI2020-112108 is part of the ERA-NET Cofund BlueBio Programme supported by the European Union.

Conflict of interest

The authors declare no conflict of interest.

References

[1] J. Gómez-Morales, C. Verdugo-Escamilla, R. Fernández-Penas, C. Maria Parra-Milla, C. Drouet, M. Iafisco, F. Oltolina, M. Prat, J.F. Fernández-Sánchez, Journal of Colloid and Interface Science 538 (2019) 174–186.

[2] V.K.A. Sreenivasan, A. V Zvyagin, E.M. Goldys, Journal of Physics: Condensed Matter 25 (2013) 194101.

[3] J. Li, J.-J. Zhu, Analyst 138 (2013) 2506–2515.

[4] D. Saini, Gunture, J. Kaushik, R. Aggarwal, K.M. Tripathi, S.K. Sonkar, ACS Applied Nano Materials 4 (2021) 12825–12844.

[5] Y.-P. Sun, B. Zhou, Y. Lin, W. Wang, K.A.S. Fernando, P. Pathak, M.J. Meziani, B.A. Harruff, X. Wang, H. Wang, P.G. Luo, H. Yang, M.E. Kose, B. Chen, L.M. Veca, S.-Y. Xie, J Am Chem Soc 128 (2006) 7756–7757.

[6] I.A. Neacsu, A.E. Stoica, B.S. Vasile, E. Andronescu, Nanomaterials 9 (2019).

[7] B. Kasemo, Surface Science 500 (2002) 656–677.

[8] Y.Y. Hu, A. Rawal, K. Schmidt-Rohr, Proc Natl Acad Sci U S A 107 (2010) 22425–22429.

[9] J. Gómez-Morales, M. Iafisco, J.M. Delgado-López, S. Sarda, C. Drouet, Progress in Crystal Growth and Characterization of Materials 59 (2013) 1–46.

[10] I. Ortiz-Gómez, G.B. Ramírez-Rodríguez, L.F. Capitán-Vallvey, A. Salinas-Castillo, J.M. Delgado-López, Colloids and Surfaces B: Biointerfaces 196 (2020) 111337.

[11] H. Ito, Y. Fujishiro, T. Sato, A. Okuwaki, British Ceramic Transactions 94 (1995) 146–150.

[12] J. Gómez-Morales, C. Verdugo-Escamilla, R. Fernández-Penas, C.M. Parra-Milla, C. Drouet, F. Maube-Bosc, F. Oltolina, M. Prat, J.F. Fernández-Sánchez, RSC Advances 8 (2018) 2385–2397.

[13] T. Kataoka, K. Shinozaki, S. Abe, M. Tagaya, Journal of Physics and Chemistry of Solids 122 (2018) 218–226.

[14] N. Dhiman, S. Ghosh, Y.K. Mishra, K.M. Tripathi, Materials Advances 3 (2022) 3101–3122.

[15] J. Gómez-Morales, R. Fernández-Penas, F.J. Acebedo-Martínez, I. Romero-Castillo, C. Verdugo-Escamilla, D. Choquesillo-Lazarte, L.D. Esposti, Y. Jiménez-Martínez, J.F. Fernández-Sánchez, M. Iafisco, H. Boulaiz, Nanomaterials 12 (2022).

[16] J. Gómez-Morales, R. Fernández-Penas, I. Romero-Castillo, C. Verdugo-Escamilla, D. Choquesillo-Lazarte, A. D'Urso, M. Prat, J.F. Fernández-Sánchez, Nanomaterials 11 (2021).

[17] N. Dhiman, P. Mohanty, New Journal of Chemistry 43 (2019) 16670–16675.

[18] G.S. Das, A. Bhatnagar, P. Yli-Pirilä, K.M. Tripathi, T. Kim, Chemical Communications 56 (2020) 6953–6956.

[19] S.S. Syamchand, G. Sony, Journal of Luminescence 165 (2015) 190–215.

[20] P. Yang, Z. Quan, C. Li, X. Kang, H. Lian, J. Lin, Biomaterials 29 (2008) 4341–4347.

[21] A. Escudero, M.E. Calvo, S. Rivera-Fernández, J.M. de la Fuente, M. Ocaña, Langmuir 29 (2013) 1985–1994.

[22] A. Doat, M. Fanjul, F. Pellé, E. Hollande, A. Lebugle, Biomaterials 24 (2003) 3365–3371.

[23] Y. Jabalera, F. Oltolina, M. Prat, C. Jimenez-Lopez, J.F. Fernández-Sánchez, D. Choquesillo-Lazarte, J. Gómez-Morales, Nanomaterials (Basel) 10 (2020).

[24] L. Mino, F. Pellegrino, S. Rades, J. Radnik, V.-D. Hodoroaba, G. Spoto, V. Maurino, G. Martra, ACS Applied Nano Materials 1 (2018) 5355–5365.

[25] V. Bolis, C. Busco, P. Ugliengo, Journal of Physical Chemistry B 110 (2006) 14849–14859.

[26] P. Ivanchenko, J.M. Delgado-López, M. Iafisco, J. Gómez-Morales, A. Tampieri, G. Martra, Y. Sakhno, Scientific Reports 7 (2017).

[27] I. Hemmilä, S. Dakubu, V.M. Mukkala, H. Siitari, T. Lövgren, Anal Biochem 137 (1984) 335–343.

[28] K.P.F. Siqueira, P.P. Lima, R.A.S. Ferreira, L.D. Carlos, E.M. Bittar, F.M. Matinaga, R. Paniago, K. Krambrock, R.L. Moreira, A. Dias, The Journal of Physical Chemistry C 119 (2015) 17825–17835.

[29] J. Gómez Morales, R. Fernández Penas, C. Verdugo-Escamilla, L. Degli Esposti, F. Oltolina, M. Prat, M. Iafisco, J.F. Fernández Sánchez, Crystals 9 (2019).

[30] K.P.F. Siqueira, P.P. Lima, R.A.S. Ferreira, L.D. Carlos, E.M. Bittar, E. Granado, J.C. González, A. Abelenda, R.L. Moreira, A. Dias, Chemistry of Materials 26 (2014) 6351–6360.

[31] F.S. Richardson, Chemical Reviews 82 (1982) 541–552.

[32] C. Zollfrank, H. Scheel, S. Brungs, P. Greil, Crystal Growth & Design 8 (2008) 766–770.

[33] J.R. Lakowicz, Principles of Fluorescence Spectroscopy, 2nd ed., Kluwer Academic/Plenum Publishers, New-York, 1999.

[34] F. Arena, C. Deiana, A.F. Lombardo, P. Ivanchenko, Y. Sakhno, G. Trunfio, G. Martra, Catalysis Science and Technology 5 (2015) 1911–1918.

[35] K. Nakamoto, Infrared and Raman Spectra of Inorganic and Coordination Compounds, Fourth Edi, Wiley, New York, 1986.

[36] G.B. Deacon, R.J. Phillips, Coordination Chemistry Reviews 33 (1980) 227–250.

[37] G.N. Vayssilov, M. Mihaylov, P. St. Petkov, K.I. Hadjiivanov, K.M. Neyman, The Journal of Physical Chemistry C 115 (2011) 23435–23454.

[38] Y. Sakhno, L. Bertinetti, M. Iafisco, A. Tampieri, N. Roveri, G. Martra, Journal of Physical Chemistry C 114 (2010) 16640–16648.

[39] F. Chiatti, M. Corno, Y. Sakhno, G. Martra, P. Ugliengo, Journal of Physical Chemistry C 117 (2013) 25526–25534.

[40] Y. Sakhno, P. Ivanchenko, M. Iafisco, A. Tampieri, G. Martra, Journal of Physical Chemistry C 119 (2015) 5928–5937.

[41] K.I. Hadjiivanov, G.N.B.T.-A. in C. Vayssilov, in: Academic Press, 2002, pp. 307–511.

[42] V. Bolis, C. Busco, G. Martra, L. Bertinetti, Y. Sakhno, P. Ugliengo, F. Chiatti, M. Corno, N. Roveri, Philosophical Transactions of the Royal Society A-Mathematical Physical and Engineering Sciences 370 (2012) 1313–1336.

Supplementary information

Structural and Surface Studies of Luminescent Ca/Eu Phosphate Nanomaterials: From the Bulk to Surface Features

Pavlo Ivanchenko[1,2], Guillermo Escolano Casado[1*], Lorenzo Mino[1], Luca Dassi[1], Jorge F. Fernández-Sánchez[3], Gianmario Martra[1†], Jaime Gómez-Morales[4]

[1]Department of Chemistry and Interdepartmental Nanostructured Interfaces and Surfaces (NIS) Centre, University of Torino, via P. Giuria 7, Torino, 10125, Italy

[2]MOBI Research Group, Department of Electric Engineering and Energy Technology (ETEC), Vrije Universiteit Brussel, Pleinlaan 2, 1050 Brussels, Belgium

[3]Department of Analytical Chemistry, Faculty of Sciences, University of Granada, Avda. Fuentenueva s/n, 18071 Granada, Spain.

[4]Laboratorio de Estudios Cristalográficos. Instituto Andaluz de Ciencias de la Tierra (CSIC-UGR). Avda. Las Palmeras, nº 4. E-18100 Armilla (Granada), Spain.

*Corresponding autor: guillermo.escolanocasado@unito.it

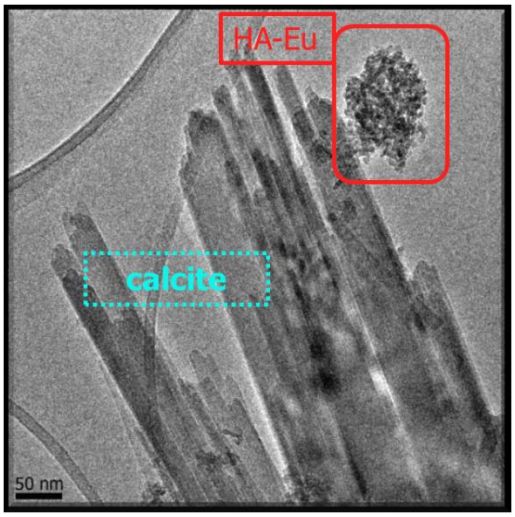

Figure S1. Low magnification TEM image showing the relative dimension of calcite and HA particles.

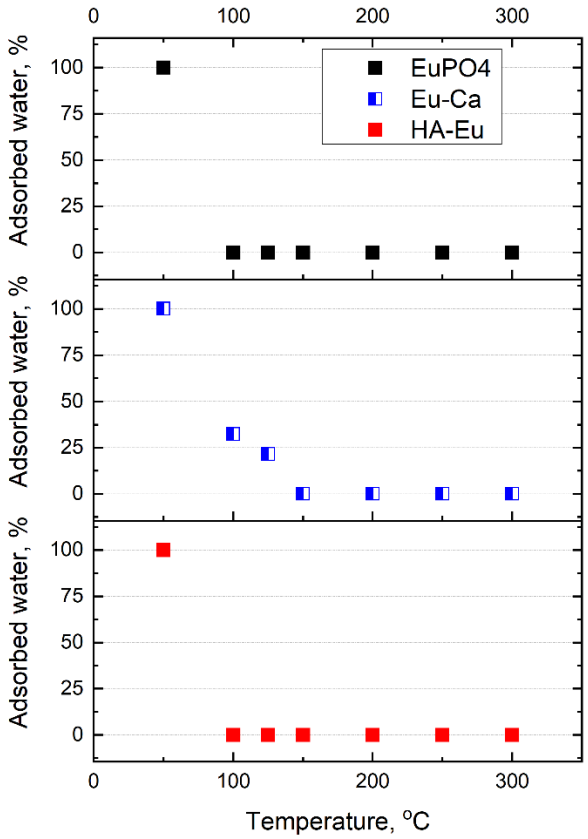

Figure S2. Relative amounts of residual water after 2 hours of outgassing at increasing temperatures.

Comment to the Figure S2.

The samples in form of self-supporting pellets were outgassed at the increasing temperatures ranging from IR beam temperature (323K) to 573K monitoring the amount of water left adsorbed after the treatment. The resulting values correspond to the relative values of the integrated intensities of the water bending mode located at 1645cm^{-1} derived from the difference spectra of a spectrum after 2 hours of outgassing and the same sample after 2 hours of outgassing followed by 10 H/D exchanges.

Table S1. Differences between the positions of the maxima of νCO in adsorbed state and gas phase.

Sample	***HA***[1]	***EuP-Ca***	***HA-Eu***	***EuP***
$\Delta(\nu CO_{ads}-\nu CO_{gas})$, cm^{-1}	26	22	17	16

[1] Y. Sakhno, P. Ivanchenko, M. Iafisco, A. Tampieri, G. Martra, J. Phys. Chem. C 119 (2015) 5928–5937.